Journal of Electron Spectroscopy and Related Phenomena 240 (2020) 146935

Contents lists available at ScienceDirect

Journal of Electron Spectroscopy and Related Phenomena

journal homepage: www.elsevier.com/locate/elspec

The effect of ion implantation on reflection electron energy loss spectroscopy: The case of Au implanted Al films

H. Trombini[a,c], M. Vos[a], G.G. Marmitt[c,1], B.P.E. Tee[b], F.F. Selau[c], A.M.H. de Andrade[c], P.L. Grande[c]

[a] Electronic Materials Engineering, Research School of Physics, Australian National University, Canberra, Australia
[b] Department of Nuclear Physics, Research School of Physics, Australian National University, Canberra, Australia
[c] Instituto de Física, Universidade Federal do Rio Grande do Sul, Porto Alegre, RS, Brazil

ARTICLE INFO

Keywords:
Reflection electron energy loss spectroscopy
Ion implantation
Electron transport in matter

ABSTRACT

Gold-implanted aluminum films are used to investigate how reflection electron energy loss spectra (REELS) change due to the presence of a small concentration of heavy atoms at a specific depth. Au ions were implanted with 30, 100 and 300 keV energy. REELS spectra were taken at energies between 10 and 40 keV. Large changes in the REELS spectra are observed after Au implantation, but the nature of the change indicates that they are not due to modification of the dielectric function of the implanted layer, but should be interpreted as changes in the partial intensities that make up the spectrum. Two models are used to describe the results quantitatively. One method assumes v-shaped trajectories (i.e. only a single elastic deflection) and the REELS spectrum can then be calculated in a closed form. The other method is a Monte-Carlo based simulation which allows for multiple elastic deflections. Both methods describe the experimental spectra quite well, but at larger energy losses significant deviations occur between the measured and calculated intensity for both the implanted and not-implanted films. The difference in the REELS spectrum before and after implantation is less affected by these discrepancies, and can be used to obtain an estimate of both the depth and concentration of the implanted Au atoms. Due to the presence of sharp plasmon features in the energy loss spectrum of aluminum the experiment can tell us directly which partial intensities are affected by the Au impurities, as the recoil energies due to elastic scattering make it possible to identify the contribution of Au to the first few plasmons. As the Au implantation fluence is known the measurement can be used to determine the ratio of the Au and Al elastic scattering cross sections, which deviates strongly from that calculated from the Rutherford formula.

1. Introduction

Understanding the propagation of energetic electrons in matter is a topic not only of fundamental importance to physics, but also has more practical ramifications for fields like electron microscopy [1], photoemission [2,3] and radiation therapy [4]. In the past most work using reflection electron energy loss spectroscopy (REELS) has focused on the interaction of fast electrons with elemental solids. This has lead to a good understanding of how the measured loss spectrum relates to the dielectric function and the corresponding inelastic mean free path (IMFP).

For higher incoming energies the recoil losses in a REELS experiment are significant and it becomes possible to determine the mass of the scattering atom [5]. The technique is then often referred to as electron Rutherford backscattering spectroscopy (ERBS). ERBS/REELS makes more detailed surface analysis experiments possible and it was used to determine e.g. the layer thickness when one compound was grown on another [6].

Here we want to study in detail the effect of impurities distributed inhomogeneously in matter on REELS/ERBS spectra, using as a test system Au-implanted aluminum samples. Aluminum was chosen as a host material as it has a very simple loss function, dominated by a single sharp plasmon, which makes, as we will see, interpretation of the results more direct. The implantation energy was such that the IMFP of the probing electrons was of the order of the range of the implanted ions. The effect of low-energy implantation in Al films, was studied by ERBS before [7]. In that case the depth of the implanted ions was much less than the IMFP of the probing electrons.

In particular high-Z impurities, with their large elastic scattering cross section should affect fast electron trajectories significantly, even

[1] Present address: University Medical Center Groningen Netherlands.

https://doi.org/10.1016/j.elspec.2020.146935
Received 16 December 2019; Received in revised form 24 January 2020; Accepted 3 February 2020
Available online 05 February 2020
0368-2048/

at low concentration. This is one of the reasons that Au nano-particles in cells are thought to locally enhance the effect of ionizing radiation [8]. Such a system is very complicated and hence simulations have been made for the more simple systems such as Au-nano particles in water, using various Monte Carlo codes in order to establish their validity [9]. However, even this simple system is hard to study experimentally by electron-spectroscopic means. In this study we show, in great detail, the effects of Au impurities in Al and show how these measurements can be used to test analytical and Monte-Carlo based descriptions of the propagation of energetic electrons in matter. As the underlying physics is the same, this rather different system could also be used to test the fundamentals incorporated in medical-physics programs such as GEANT4-DNA [10] by confronting the output of such a program directly with this experiment.

Another area of relevance of this work is *Z*-contrast microscopy [11]. The signal obtained in an electron microscope at larger scattering angle depends strongly on the atomic number of the atoms present in the sample, and increased intensity is observed in a sample at positions that contain heavy elements. In an electron microscope the focus is on spatial resolution and *Z*-contrast microscopy usually just counts the large-angle scattered electrons that emerge above a cut-off energy. Alternatively one can measure the backscattered electron intensity dependence on the electron beam energy, and obtain depth information in this way [12]. Here we explore the depth information that is present in the energy distribution of the backscattered electrons using a spectrometer that has good energy resolution for a laterally homogenous sample.

2. Experimental details

3000 Å thick Al layers were sputtered-deposited on a Si wafer. Samples were implanted with 30, 100 and 300 keV Au ions up to a fluence (as determined by RBS using 2 MeV He^+ ions) of 2.3×10^{15}, 4.1×10^{15} and 6.2×10^{15} ions/cm^2 respectively. The range based on the SRIM/TRIM software [13] (and straggling σ) of the Au distribution after implantation is at 30 keV 184 Å (43 Å), at 100 keV 318 Å (79 Å) and at 300 keV 817 Å (148 Å). TriDyn simulations [14] gave somewhat (up to ≈20%) larger depth and larger straggling values for the implanted Au ions. These differences are due to the rather large electronic stopping power TRIM uses for heavy ions at low energies [15]. From these, and an unimplanted sample, ERBS/REELS spectra were measured using incoming electrons with energies between 10 and 40 keV. The recoil effect makes it possible to identify the mass of the scattering atoms for higher incoming energies. All samples are expected to have a native aluminum oxide layer as the Al samples were introduced into the spectrometer without subsequent sputter-cleaning.

Spectra were collected for a range of energy loss values by scanning the analyzer float voltage. The analyzer is positioned at 135° with respect to the incoming beam direction. The beam current was measured and the scan would progress to the next float voltage after a preset amount of charge was collected. Beam current varied between 2 nA at 10 keV incoming energy up to 10 nA at 40 keV. The energy resolution was better than 0.5 eV but Doppler broadening due to atomic motion affects the width of the elastic peak for higher incoming energies, especially for Al and O.

3. Experimental results

Examples of some of the obtained results are shown in Fig. 1 for the three implanted samples and are compared with those of the not-implanted sample. Here the incoming beam (E_0 = 40 keV) was incident along the surface normal. The spectra were aligned such that the main elastic peak (corresponding to Al) is at the calculated recoil energy, which is 2.88 eV for electrons scattering over 135°. The Au implantation affects the obtained intensity over a wide energy loss range. The elastic peak (Fig. 1, left panel) after implantation shows a new sharp feature at near zero energy loss corresponding to electrons backscattering from Au.

Note the small tail at the low energy side on the right of the Al elastic peak. It is due to oxygen that is part of a thin (≈3 nm) Al_2O_3 layer, that always forms when an Al film is exposed to atmosphere. After implantation this feature is ≈10% more intense i.e. the native oxide layer has grown slightly during implantation as a consequence of ion-beam mixing.

In the following we refer to the contribution to the spectrum of electrons backscattered from element *x* after *n* inelastic losses as $I_x^{(n)}$. I_{Au}^0 is most intense (relative to I_{Al}^0) for the low-energy implantation (in spite of its lower fluence). I_{Au}^0 decreases for increasing implantation energy as the Au becomes deeper, and hence I_{Au}^0 is heavily affected by attenuation the higher implantation energies.

At larger energy losses we see additional loss features (Fig. 1, central panel). The first feature, a double peak, is at 15 eV below the elastic peak of Au and Al. The two components, 2.5 eV apart, are separated by the same energy difference as the Au and Al elastic peak and are attributed to electron trajectories that created a single plasmon and scattered from either from Au (intensity I_{Au}^1) or Al (intensity I_{Al}^1). Note that the intensity ratio for these two peaks I_{Au}^1: I_{Al}^1 is very different from the intensity ratio of the elastic peaks. Whereas I_{Au}^0 for 30 keV implantation was the most intense, I_{Au}^1 is most intense for the 100 keV implantation. The I_{Au}^1 at 300 keV implantation energy is half the intensity of I_{Au}^1 at 30 keV, whereas I_{Au}^0 at 300 keV implantation was 6 times less intense than I_{Au}^0 for the 30 keV implantation. These are all consequences of the different Au depth distributions for the different Au implantation energies (and their respective fluence).

As the second plasmon feature is broader than the first, the contribution of electrons scattered from Au and Al is here only partly resolved. I_{Au}^2 is the weakest for the 30 keV implantation, whereas it is of comparable magnitude for the 100 and 300 keV implantation.

Note that, if we overlay a spectrum of a pure Al film, in such a way that the Al elastic peak before and after implantation have the same area, then the plasmon feature of the non-implanted film coincides closely to the peak associated with $I_{Al}^{1,2}$ in the implanted film. This is to be expected as the aluminum concentration varies only slightly due to the presence of the Au impurities (from 100% at the surface and very large depth to 97–98% at the depth with the maximum Au concentration). We see thus no clear evidence that the loss function itself has changed due to the implantation.

At even larger energy losses (right panel of Fig. 1) the plasmon gets too wide to clearly distinguish the contribution of electrons scattered from Al and Au anymore. However, the contribution of Au at larger losses can still be discerned by comparing the measured intensity of the loss spectrum with that of a pure Al film. For the 30 keV implantation the enhanced intensity is clearly significant up to 60 eV energy loss, up to 300 eV for the 100 keV implantation, and extends outside the measured range (700 eV) for the 300 keV implantation.

4. Calculations

We present two calculations, one 'analytical' and one Monte-Carlo based. The 'analytical' model assumes only a single (large-angle) elastic scattering event, the Monte Carlo approach allows for multiple elastic scattering. Both approaches calculated the inelastic losses in the aluminum film using the dielectric formalism. Both calculations also assume that a limited concentration of Au atoms (a few %) in an aluminum film does not affect its dielectric function. If knowledge of how the dielectric function changes with Au concentration was available, it could be straight-forwardly incorporated in the Monte Carlo simulation, but not as easily in the 'analytical' approach. We used the parameterization of Sun et al. [16] of the dielectric function for Al in the optical limit, but we increase the width of the main plasmon peak at 15.055 eV from 0.642 eV to 1 eV, as this improved the description of the spectra for our sputter-deposited Al films. Extending the dielectric

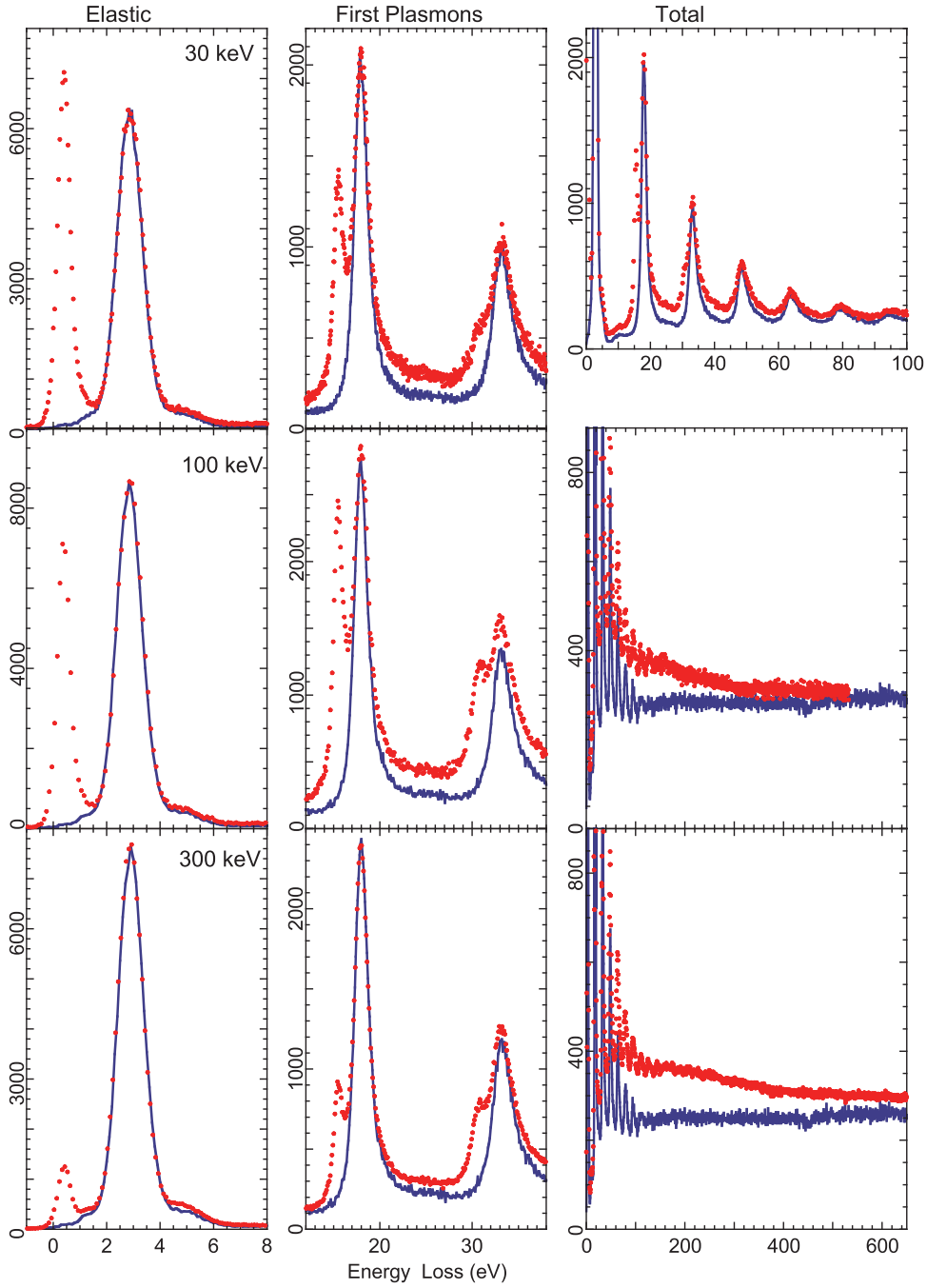

Fig. 1. 40 keV ERBS/REELS spectra of the elastic peak (left), first two plasmons (center) and the whole energy loss range (right) for three implantation energies as indicated (red dots). The spectra without Au implantation are presented by the blue lines. The calculated recoil losses are for Au 0.40 eV, Al 2.88 eV and O 4.86 eV and compare well with the experimentally observed elastic peak positions.

function away from zero momentum (i.e. away from the optical limit) was done using the Mermin approach [17]. From the dielectric function we calculate for various projectile energies the differential inelastic inverse mean free path in the usual way [2], and the corresponding IMFP λ. Dividing the differential inverse inelastic mean free path by λ one obtains the normalized differential inverse inelastic mean free path (NDIIMFP) which is the probability distribution that in an inelastic event a certain amount of energy is lost. In the next paragraphs we give some details specific for each model.

4.1. Analytical calculation within the v-shape approximation

This model was described recently in the context of Au implanted SiO_2 layers [18]. We reproduce the description here for completeness.

Assuming only a single large-angle deflection (i.e. a v-shaped trajectory), the total path length is related to the scattering depth z by:

$$L = z/\cos(\theta_0) + z/\cos(\theta_1) = \alpha z \quad (1)$$

with α describing the relation between L and z and $\theta_{0,1}$ are the angle of the incoming and detected outgoing electrons with the surface normal. The assumption of v-shaped trajectories also underlies the interpretation of almost all ion-beam based RBS measurements.

The probability of backscattering from depth z is proportional to the Al concentration times its differential cross section (DCS) for scattering over 135° plus the Au concentration weighted by its DCS at that angle. Theses DCS values were obtained from the ELSEPA package [19]. As the

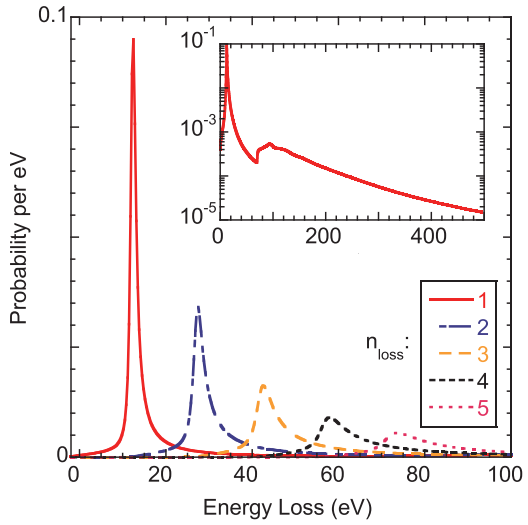

Fig. 2. The energy distribution of electrons after n energy loss events in Al, calculated for 40 keV electrons based on the dielectric function of Ref. [16]. The insert shows the distribution for $n = 1$ on a log scale over an extended energy range.

Au DCS is 2 orders of magnitude larger than the Al DCS even a small Au concentration (a few %) has a significant effect of the backscatter probability.

For a trajectory with length L the probability that n inelastic events occurred is given by the Poisson distribution:

$$p_n(L) = \frac{(L/\lambda)^n}{n!} e^{-L/\lambda} \tag{2}$$

The contribution to the spectrum of trajectories with n inelastic losses has a shape proportional to the $(n-1)$ times self-convolution of the NDIIMFP. These distributions are plotted in Fig. 2. All curves have unit area. The maximum height of these distribution decreases with increasing n for two reasons. Firstly, the distribution broadens with increasing n. Secondly, the fraction of the NDIIMFP that is part of the tail extending to larger energies is significant. This tail is due to the excitation of semi-core electrons (2s and 2p for Al). The area corresponding to losses less than 30 eV (i.e. the main plasmon peak) is ≈80%. Thus the likelihood that if n excitations occur all energy losses can be considered as plasmons is 0.8^n, which becomes a small number for large n. Hence the plasmon peak is not as dominant after $(n-1)$-fold convolution.

The number of electrons backscattered from Au and Al at depth z is calculated separately based on the concentration of that element at depth z and their cross section. The fraction of this intensity with n losses is calculated from Eq. (2). The shape of the contribution of atoms at depth z is then obtained by adding the $n-1$-fold convolutions of the NDIIMFP weighted by their Poisson fraction.

We have to take into account the recoil losses due to the elastic scattering event. The recoil losses of element x are centered around its mean recoil energy $\bar{E}_r^x = q^2/2M_x$ with M_x the mass of the atom and q the momentum transfer for scattering over 135° (for $E_0 = 40$ keV $q = 193$ Å^{-1}, in good approximation independent of M_x). The recoil losses for scattering from Al are thus larger than for Au, due to its smaller mass. The recoil losses are taken to have a Gaussian distribution, due to the atomic motion (Doppler broadening). The width (σ) of this Gaussian distribution is given by [20]:

$$\sigma = \sqrt{\frac{4}{3}\bar{E}_r^x \; K_e(x)} \tag{3}$$

with $K_e(x)$ the mean kinetic energy of element x. As the Debye temperature of Al is not too large (428K) we assumed a mean kinetic energy of Al (at ambient temperature) to be slightly more than $3/2\,kT$ and used a value of K_e(Al) = 40 meV in the simulation. The same value was used for Au. For Au the Doppler broadening is of the order of the experimental resolution and it is hard to determine thermal and experimental contribution to the observed width separately. The Al elastic peak is clearly wider than the Au elastic peak, and the simulation using the above values reproduces the experiment quite well.

Finally, the experimental spectrum is then obtained by adding the Al and Au contribution, integrated over all z.

4.2. Monte-Carlo based approach

The Monte Carlo program used was PM3 [21,22]. It uses a variation on the trajectory reversal approach [23] to connect incoming and outgoing electron trajectories. One set of electron trajectories is simulated for electrons impinging on the sample from the electron gun and a set for electrons emerging from the analyzer. The contribution of a specific incoming and outgoing trajectory combination at depth z from atom A is proportional to the cross section of atom A for scattering over the angle between the incoming and (time-reversed) outgoing electron trajectory and the concentration of that element. Energy losses due to inelastic excitation and atomic recoils are calculated using standard Monte Carlo techniques and the mentioned dielectric function [24]. The probability of deflection of an electron is determined from the differential elastic cross section, as calculated again from ELSEPA cross sections.

In this approach we define (besides layers of pure Al) a number (usually 3) of slabs with varying Au concentration. The total number of Au atoms in these slabs, is chosen so it corresponds with the implantation fluence, and the depth is chosen according to the range and width of the ion distribution obtained from SRIM/TRIM or TridDyn.

The effect of the native oxide layer at the surface of aluminum can be incorporated in the Monte Carlo calculation as an additional 30 Å Al_2O_3 layer. Also for Al_2O_3 we use the parameterization of its dielectric function as given by Sun et al. [16].

4.3. Comparing calculations with experiment

Monte Carlo Simulations and v-shape model calculations were done for both pure aluminum and Au implanted aluminum, and the result is compared to the measurement in Fig. 3. The Monte Carlo and v-shape calculations give very similar results. The v-shape approach does not include the surface oxide layer and hence the shoulder near 5 eV energy loss (corresponding to electrons scattered from O) in the elastic peak is missing. Both approached show that the first two plasmon features are split when Au is implanted and the calculated intensities of $I_{\mathrm{Au}}^{1,2}$ are comparable to that of the experiment. The v-shape approach underestimates the intensity somewhat for 50 eV energy loss and above for both the implanted and non-implanted sample, whereas Monte Carlo method overestimates the intensity for losses larger than 100 eV (not shown in the figure).

It is tempting to conclude from the results of Fig. 3 that the PM3 calculation is better than the v-shape calculation. However, by changing slightly the dielectric function used one can bring the v-shape calculation better in agreement with the experiment than the PM3 simulation. The outcome of the comparison is very sensitive to the amount of 'tail' in the dielectric function used [25]. The (non-trivial) implementation of the trajectory-reversal approach in PM3 clearly works well for shorter trajectories (i.e. the low energy loss part of the spectrum), but for longer trajectories (larger losses) it is harder to identify if deviations of simulations and experiments are due to shortcomings in the dielectric function used, or limitations in the way incoming and outgoing trajectories are combined within the trajectory reversal algorithm.

For the v-shape model it was possible to take the Au concentration to be the spectrum either as a continuously varying Gaussian or as a three-layer system. Nearly identical results were obtained. It is thus not

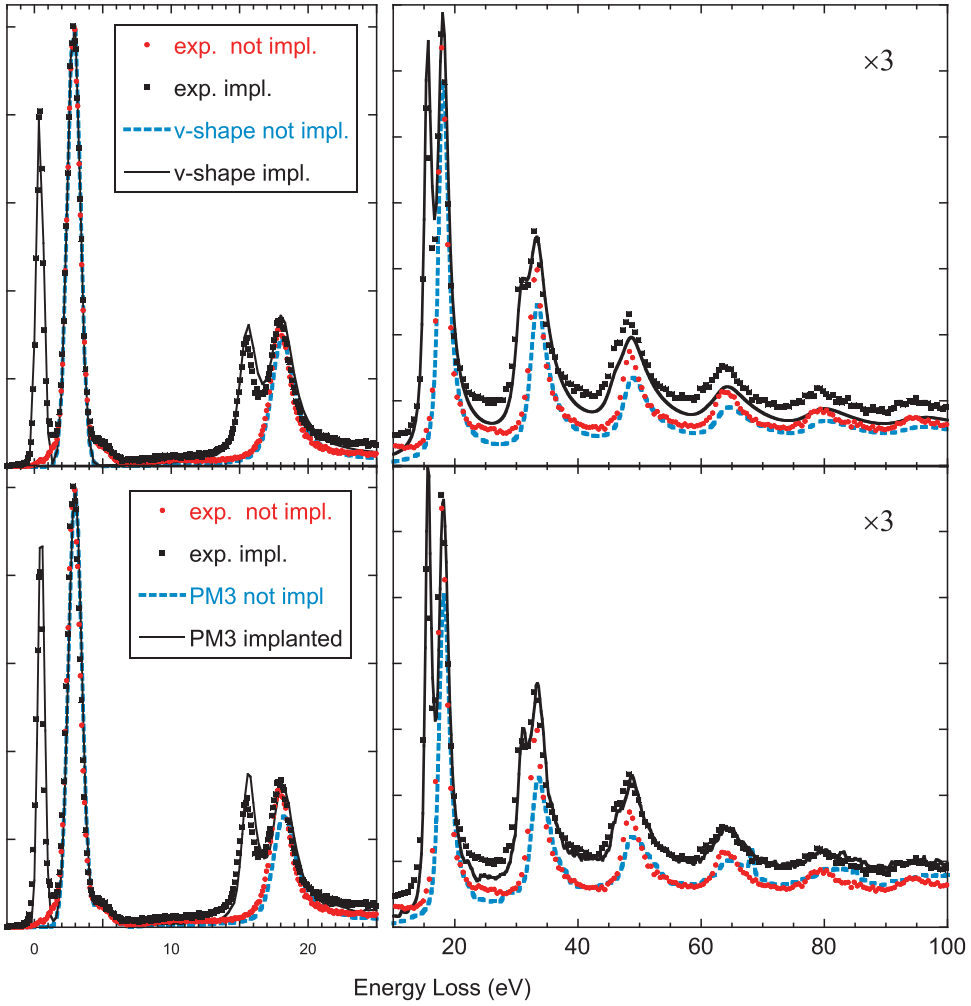

Fig. 3. A comparison of the results of 100 keV Au implanted sample with the v-shape (top) and PM3 (bottom) calculations.

expected that the Monte Carlo simulation would change if the Au distribution was modeled by more than 3 layers.

For the 100 keV Au implanted samples we studied the dependence of the spectra on the incoming energy using values of E_0 of 10, 20, 30 and 40 keV. The results are compared in Fig. 4. With decreasing incoming energies the IMFP decreases and one probes for small loss values mainly the depth before the region containing Au atoms. As a consequence the relative intensity of the Au elastic peak is reduced by a factor of 2.5 at 20 keV relative to 40 keV. With decreasing incoming energy the recoil splitting of the Au and Al elastic peak decreases as well. At 10 keV the two elastic peaks have merged and it is thus not possible to normalize the elastic peak area of Al to the same area when comparing the implanted and non-implanted samples. Instead the total elastic peak was used for normalization as the Au contribution should be small here. Using this normalization it is clear that the intensity at larger losses is larger for the implanted sample, i.e. Au contributes more at larger losses than to the elastic peak.

These measurements were simulated as well with the v-shape method and the PM3 program. Within the v-shape program one can get the intensity of the electrons scattered from Al and Au separately and at 10 keV the calculated Au contribution to the elastic peak was less than 5%, showing that the error in including the Au contribution in the elastic peak normalization is minor.

Overall the calculations reproduce the experiment quite well. For smaller E_0 values PM3 seems to overestimate both the Al and Au contribution at larger energy losses, and here the v-shape calculations seem to agree better.

Another way to change the spectra is by varying the geometry. In Fig. 5 we show the results for 40 keV incoming energy for the case of the 300 keV implanted sample as a function of the sample rotation. The incoming angle (relative to the surface normal) was varied from -30° to 80° and the angle of the outgoing angle varied then from −85° to 35°. Thus for the first sample orientation we are very surface-sensitive because the outgoing electrons are glancing with the surface, and for the last measurement we are again surface sensitive, but now because the incoming angle is glancing. In between we are in more bulk-sensitive geometries. Indeed, the Au-derived elastic peak and the corresponding first plasmon peak are more strong for the intermediate angles as expected for this high-energy implanted sample. In contrast, the O contribution of the Al_2O_3 surface layer is weakest for the intermediate angles showing that the oxygen atoms are, as expected, close to the surface. All these measurements were simulate with the PM3 program, and as can be seen in Fig. 5 as well the simulations reproduce this angular dependence quite well.

5. Discussion

One way of looking at these measurements is that the Au atoms enhance the number of electrons backscattered from a certain depth. If one simplifies by assuming that all Au atoms are at the mean implantation depth D than, within the v-shape approximation all extra intensity corresponds to a path length of αD (see Eq. (1)).

In Fig. 6 we plot the additional intensity (i.e. the difference of the measured implanted and non-implanted spectra, normalized as in

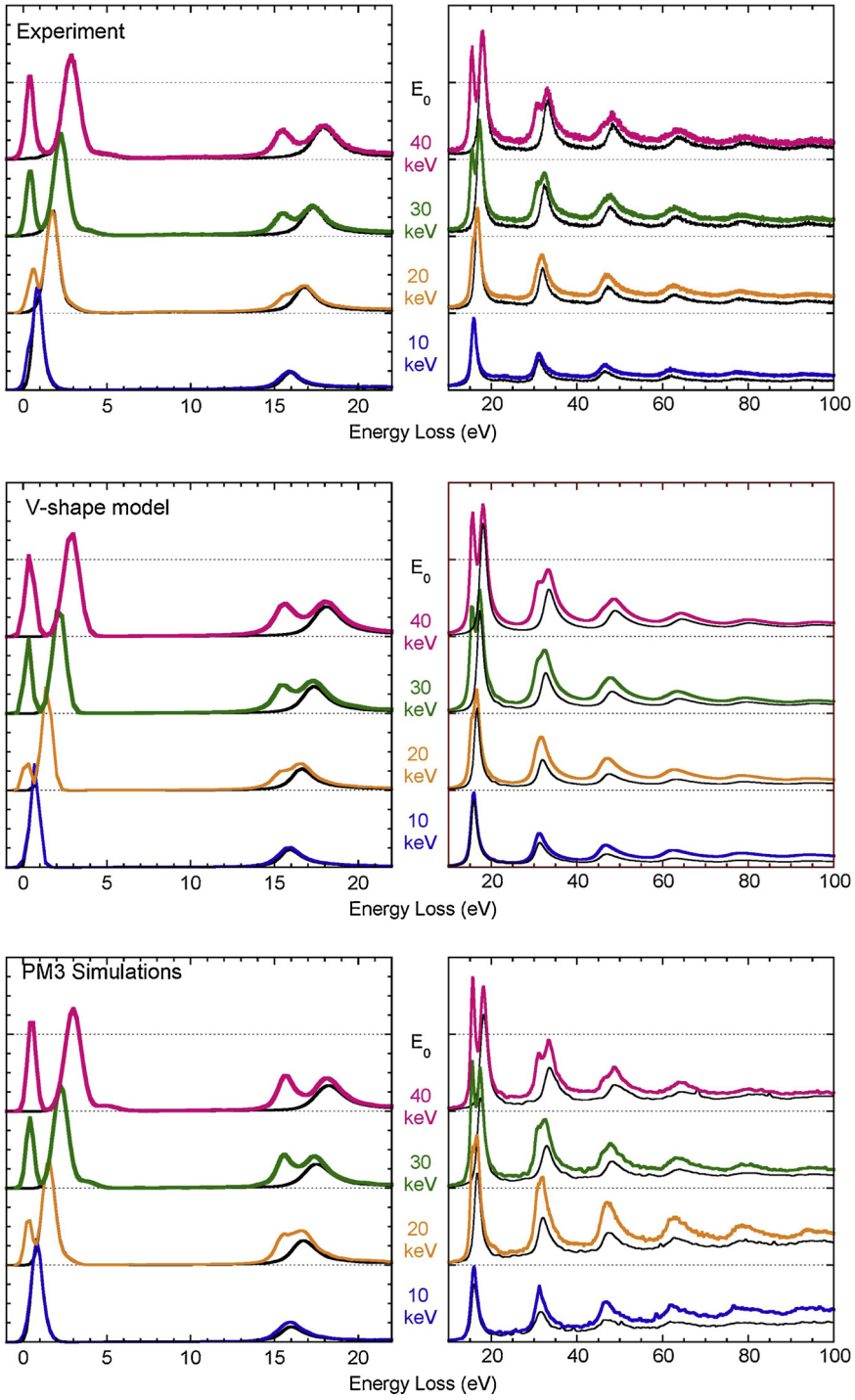

Fig. 4. The measured spectra of an Al film before (black) and after 100 keV Au implantation with (color) for electron energies as indicated. Left panels: elastic peak and first plasmon, right panel: larger energy loss area. The top panels are the experimental results, the central panels are based on the v-shape approximation and the lower panels are the results of the PM3 simulations. The Al_2O_3 layer was included in the PM3 simulation, but not considered in the v-shape calculation.

Fig. 1) together with the contribution of the Au atoms, as calculated within the v-shape model. The insert shows the partial intensities as calculated from Eq. (2) for αD with D the mean depth as calculated with TRIM. With increasing implantation energy the Poisson distribution maximum shifts to larger values, i.e. the contribution of higher partial intensity increases with increasing implantation energy. For the case of Al, with its sharp well-defined plasmon, one can distinguish a signature of each partial intensity as long as the corresponding plasmon can be identified. For the 30 keV implantation the first 2 plasmons can be seen clearly in the difference spectrum, while for 100 keV the first 4, and for 300 keV the first 6–7 plasmons can be seen. The height of the plasmon peak decreases, however faster than the partial intensities. E.g. at 300 keV implantation the partial intensity has a maximum for $n = 4$ whereas the first plasmon appears the strongest in the experiment. This apparent contradiction can be understood by observing the shape of the NDIIMFP (see Fig. 2). The maximum height of the NDIIMFP decreases rapidly with n. This explains why, for the 300 keV implantation, where the 4th partial intensity should be strongest, the 4th plasmon only appears as a relatively weak feature. For the 300 keV case we used the TriDyn depth in the calculation as it compares better with the

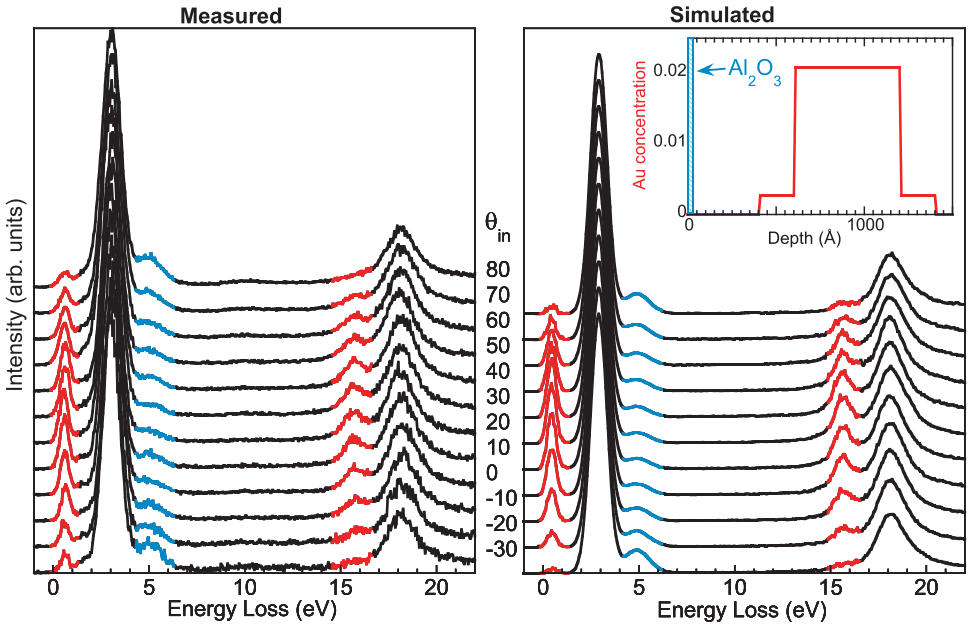

Fig. 5. Angular dependence of the yield as measured and simulated using PM3. Part of the spectrum that is mainly due to Au is color-coded red, due to oxygen blue. The insert shows the Au concentration profile assumed in the simulation.

experiment, for the lower implantation energies the difference is the calculated spectra using TriDyn or SRIM/TRIM is small. The larger implantation depth (compared to SRIM/TRIM) for 300 keV was also supported by (ion-based) RBS measurements.

In these calculations we assumed that the ratio of the differential cross section of Au and Al for scattering over 135° as calculated by ELSEPA is correct. Although the theoretical justification of the ELSEPA program is sound, the comparison with experimental data of differential cross sections for large scattering angles and energies well above 1 keV are mainly lacking [19], but more recently an experimental comparison was made, based on recoil-separated elastic peaks in oxide compounds with well-defined stoichiometry [26]. Under the conditions described here, the Al differential cross section is close to the one obtained by the Rutherford formula, indicating that one is close to the high-energy limit where the screening by the Al electrons is not important. The Au cross section is, however, strongly enhanced compared to Rutherford, and in that case the atomic electrons have thus a strong influence. The case of Au is of interest as it has a larger Z than any of the elements reported in Ref. [26] and the enhancement is expected to be strongest. One could determine from these measurement the Au cross section (relative to the one of Al). The ratio of the Au to Al DCS at this angle and energy is according to ELSEPA DCS(Au)/DCS(Al) = 87.4 whereas from the Rutherford formula is given by $(Z_{Au}/Z_{Al})^2 = 36.9$. The enhancement of the DCS ratio is thus 2.4 compared to Rutherford.

Experimentally, these cross sections can be most easily tested for the low-energy (30 keV) implantation case where the v-shape model is most accurate, as the path-lengths involved are small. The additional area (within the v-shape model) is proportional to the number of Au atoms present. How this extra area is divided over the elastic peak and the first plasmon peak etc. is determined by the ratio of the implantation depth and the electron mean free path. From the experimental ratio and the nominal implantation dose we obtain an enhancement of a factor 2.4, if we compare the measured and calculated ratio over the first 50 eV, exactly as predicted by ELSEPA. This method depends on how accurate the IMFP is known, as the Al intensity is proportional to λ. We plan to use this method for studying elastic scattering cross sections more systematically in the future.

Note that the momentum transfer in these backscattering experiments ($q = 193$ Å^{-1} for $E_0 = 40$ keV) is about two orders of magnitude larger than those used in high-angle annular dark-field imaging in a Transmission electron microscope (TEM). For dark-field TEM images the cross section is reduced relative to Rutherford, especially for heavy elements [27–29] and for the TEM conditions the picture that the nuclear charge is screened by inner-core electrons describes the experimentally observed cross sections well.

6. Conclusion

In this paper we have shown that incorporation of heavy impurities (up to ≈2%) at a certain depth (here done by ion implantation) changes the REELS spectrum in a major way. With increasing depth of the impurities the changes of the REELS spectrum extends to larger losses. These changes are not thought to be caused by changes in the dielectric function due to the impurities (or lattice defects introduced by the implantation), but to changes in the number of electrons that backscatter from the depth of the Au impurities. Indeed the measurements can be reproduced quite well assuming an unchanged dielectric function but incorporating the effect of the increased elastic cross section of Au impurities present at a known depth with a known concentration.

Two models were applied, one ‘analytical’, assuming only a single large-angle elastic deflection and one based on Monte Carlo simulations. The contribution of electrons scattered from Au can be identified in the spectra directly for the elastic peak and the first 2 plasmon losses as then their contribution to the spectrum is clearly separated due to the recoil effect. Agreement between the two methods and the experiment is very good for the smaller losses, but for larger losses (over 100 eV) differences are found both for pure Aluminum and Au implanted aluminum. Taking the difference between both measurements (i.e. considering only the extra intensity due to Au) a large part of these discrepancies disappears.

These experiments show detailed understanding one can get from comparing the results of REELS measurement of a sample with composition varying in depth. The Monte Carlo program is voxel based, which means we can also study samples with compositions that not only change with depth but also laterally. Such studies are currently been undertaken for samples with fin-like structures similar to those found in FinFET transistors

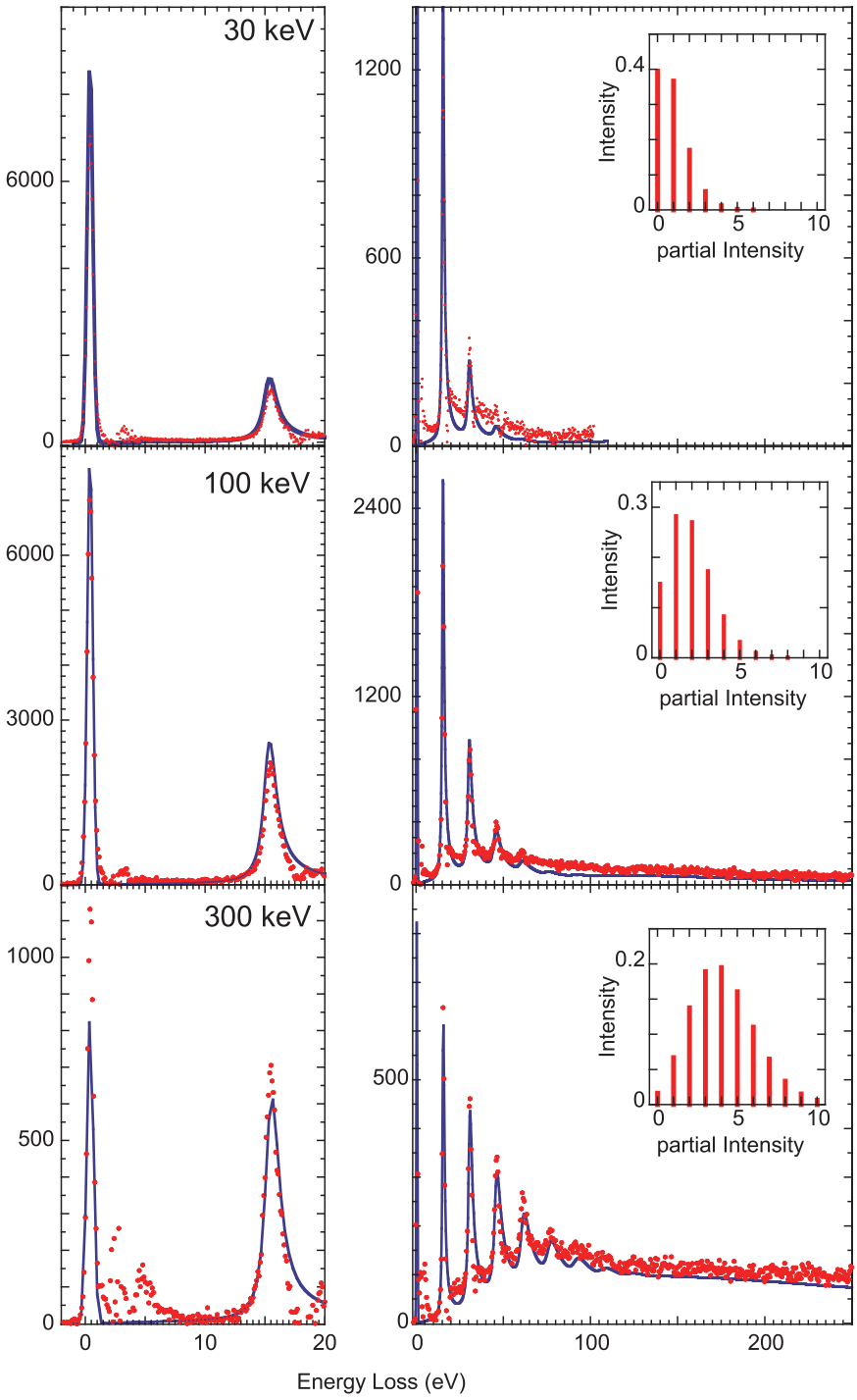

Fig. 6. The difference between the implanted and not implanted samples (dots) compared to the calculated contribution to the REELS spectrum from electrons backscattered from Au using the v-shape model. The insert shows the calculated contribution of the different partial intensities for a path length corresponding to backscattering from the mean depth Au atoms at that implantation energy.

Acknowledgements

This work was performed under the auspices of Brazilian Coordination for the Improvement of Higher Education Personnel (CAPES, 88887.176042/2018-00), Brazilian National Council for Scientific and Technological Development (CNPq, 117750/2017-4 and 1165047/2015-1), the Brazilian National Institute of Surface Engineering (INES) and PRONEX-FAPERGS. MV acknowledges support of the CAPES-PRINT program grant no.88887.372195/2019-00.

References

[1] R.F. Egerton, Electron Energy-Loss Spectroscopy in the Electron Microscope, 3rd edition, Plenum Press, New York, 2011, https://doi.org/10.1007/978-1-4419-9583-4.
[2] W.S.M. Werner, Electron transport in solids for quantitative surface analysis, Surf. Interface Anal. 31 (2001) 141, https://doi.org/10.1002/sia.973.
[3] Y.-T. Cui, S. Tougaard, H. Oji, J.-Y. Son, Y. Sakamoto, T. Matsumoto, A. Yang, O. Sakata, H. Song, I. Hirosawa, Thickness and structure of thin films determined by background analysis in hard X-ray photoelectron spectroscopy, J. Appl. Phys. 121 (2017) 225307, https://doi.org/10.1063/1.4985176.
[4] H. Nikjoo, S. Uehara, D. Emfietzoglou, Interaction of Radiation With Matter, CRC Press, 2012.

[5] M. Went, M. Vos, Investigation of binary compounds using electron Rutherford backscattering, Appl. Phys. Lett. 90 (2007) 072104, https://doi.org/10.1063/1.2535986.
[6] G. Marmitt, L. Rosa, S. Nandi, M. Vos, Analysis of multi-layer ERBS spectra, J. Electron Spectrosc. Relat. Phenom. 202 (2015) 26, https://doi.org/10.1016/j.elspec.2015.02.009.
[7] M. Went, M. Vos, Electron Rutherford backscattering case study: oxidation and ion implantation of aluminium foil, Surf. Interface Anal. 39 (2007) 871–876.
[8] S. Jain, D.G. Hirst, J.M.O. Sullivan, Gold nanoparticles as novel agents for cancer therapy, Br. J. Radiol. 85 (2012) 101, https://doi.org/10.1259/bjr/59448833.
[9] D. Sakata, I. Kyriakou, H.N. Tran, M.-C. Bordage, A. Rosenfeld, V. Ivanchenko, S. Incerti, D. Emfietzoglou, S. Guatelli, Electron track structure simulations in a gold nanoparticle using Geant4-DNA, Phys. Med. 63 (2019) 98, https://doi.org/10.1016/j.ejmp.2019.05.023.
[10] S. Incerti, I. Kyriakou, M.A. Bernal, M.C. Bordage, Z. Francis, S. Guatelli, V. Ivanchenko, M. Karamitros, N. Lampe, S.B. Lee, S. Meylan, C.H. Min, W.G. Shin, P. Nieminen, D. Sakata, N. Tang, C. Villagrasa, H.N. Tran, J.M.C. Brown, Geant4-DNA example applications for track structure simulations in liquid water: a report from the Geant4-DNA project, Med. Phys. 45 (2018) e722–e739, https://doi.org/10.1002/mp.13048.
[11] E. Rau, H. Hoffmeister, R. Sennov, H. Kohl, Comparison of experimental and Monte Carlo simulated BSE spectra of multilayered structures and in-depth measurements in a SEM, J. Phys. D: Appl. Phys. 35 (2002) 1433, https://doi.org/10.1088/0022-3727/35/12/322.
[12] M. de Goede, E. Johlin, B. Sciacca, F. Boughorbel, E.C. Garnett, 3D multi-energy deconvolution electron microscopy, Nanoscale 9 (2017) 684, https://doi.org/10.1039/c6nr07991a.
[13] J. Ziegler, M. Ziegler, J. Biersack, SRIM – the stopping and range of ions in matter (2010), Nucl. Instrum. Methods Phys. Res. Sect. B: Beam Interact. Mater. Atoms 268 (11–12) (2010) 1818–1823, https://doi.org/10.1016/j.nimb.2010.02.091.
[14] W. Möller, W. Eckstein, Tridyn – a TRIM simulation code including dynamic composition changes, Nucl. Instrum. Methods Phys. Res. Sect. B: Beam Interact. Mater. Atoms 2 (1984) 814, https://doi.org/10.1016/0168-583x(84)90321-5.
[15] K. Jin, Y. Zhang, Z. Zhu, D.A. Grove, H. Xue, J. Xue, W.J. Weber, Electronic stopping powers for heavy ions in SiC and SiO_2, J. Appl. Phys. 115 (2014) 44903, https://doi.org/10.1063/1.4861642.
[16] Y. Sun, H. Xu, B. Da, S. feng Mao, Z. jun Ding, Calculations of energy-loss function for 26 materials, Chin. J. Chem. Phys. 29 (2016) 663, https://doi.org/10.1063/1674-0068/29/cjcp1605110.
[17] N. Mermin, Lindhard dielectric function in the relaxation-time approximation, Phys. Rev. B 1 (1970) 2362–2363, https://doi.org/10.1103/physrevb.1.2362.
[18] H. Trombini, M. Vos, R. Eliman, P. Grande, Depth profiling of ion implanted samples by high-energy electron scattering, J. Phys. D: Appl. Phys. 53 (2020) 135304 https://doi.org/10.1088/1361-6463/ab66d8.
[19] F. Salvat, A. Jablonski, C.J. Powell, ELSEPA Dirac partial-wave calculation of elastic scattering of electrons and positrons by atoms, positive ions and molecules, Comput. Phys. Commun. 165 (2005) 157–190, https://doi.org/10.1016/j.cpc.2004.09.006.
[20] M. Vos, G. Marmitt, Y. Finkelstein, R. Moreh, Determining the band gap and mean kinetic energy of atoms from reflection electron energy loss spectra, J. Chem. Phys. 143 (2015) 104203, https://doi.org/10.1063/1.4929911.
[21] G. Marmitt, Metal Oxides of Resistive Memories Investigated by Electron and Ion Backscattering (PhD thesis), Universidade Federal do Rio Grande do Sul, 2017, https://www.lume.ufrgs.br/bitstream/handle/10183/170451/001053460.pdf?sequence=1.
[22] http://tars.if.ufrgs.br/.
[23] W. Werner, Trajectory reversal approach for electron backscattering from solid surfaces, Phys. Rev. B 71 (2005) 115415, https://doi.org/10.1103/physrevb.71.115415.
[24] R. Shimizu, Z.-J. Ding, Monte Carlo modelling of electron-solid interactions, Rep. Prog. Phys. 55 (1992) 487, https://doi.org/10.1088/0034-4885/55/4/002.
[25] M. Vos, P. Grande, G. Marmitt, The influence of shallow core levels on the shape of REELS spectra, J. Electron Spectrosc. Relat. Phenomena 229 (2018) 42–46, https://doi.org/10.1016/j.elspec.2018.09.006.
[26] P.L. Grande, M. Vos, Exploring the Barkas effect with keV-electron scattering, Phys. Rev. A 88 (2013) 052901, https://doi.org/10.1103/PhysRevA.88.052901.
[27] K. Iakoubovskii, K. Mitsuishi, Elastic scattering of 200 keV electrons in elemental solids: experimental observation of atomic-number-dependent oscillatory behavior, J. Phys.: Condens. Matter 21 (2009) 155402, https://doi.org/10.1088/0953-8984/21/15/155402.
[28] O.L. Krivanek, M.F. Chisholm, V. Nicolosi, T.J. Pennycook, G.J. Corbin, N. Dellby, M. Murfitt, C.S. Own, Z.S. Szilagyi, M.P. Oxley, S.T. Pantelides, S.J. Pennycook, Atom-by-atom structural and chemical analysis by annular dark-field electron microscopy, Nature 464 (2010) 571–574, https://doi.org/10.1038/nature08879.
[29] M. Treacy, Z dependence of electron scattering by single atoms into annular dark-field detectors, Microsc. Microanal. 17 (2011) 847–858, https://doi.org/10.1017/s1431927611012074.